Measurement of the neutron flux in the NEAR station at n_TOF by multi-foil activation technique

M. Mastromarco[1,2], **N. Patronis**[3,4], **S. Goula**[4], **M.E. Stamati**[3,4],
P. Torres-Sánchez[5], **D. Chiesa**[6,7]

[1]Istituto Nazionale di Fisica Nucleare, Sezione di Bari, Italy
[2]Dipartimento Interateneo di Fisica, Università degli Studi di Bari, Italy
[3]European Organization for Nuclear Research (CERN), Switzerland
[4]University of Ioannina, Greece
[5]Instituto de Física Corpuscular, CSIC-University of Valencia, Valencia, Spain
[6]Dipartimento di Fisica, Università degli Studi di Milano - Bicocca , Milano I-20126, Italy
[7]INFN - Sezione di Milano Bicocca, Milano I-20126, Italy

Abstract Insert your abstract here. Include keywords, PACS and mathematical subject classification numbers as needed.

Keywords First keyword · Second keyword · More

1 Introduction (Nikolas, Nicola)

The n_TOF facility is CERN's neutron spallation source that was conceptualised in 1998 and has been operated by the n_TOF collaboration since 2001 [1]. Since then and up to now high precision nuclear data are produced for neutron-induced reactions data for a variety of fields in nuclear physics, both in fundamental research as well as for energy, medical and other applications [2–5]. The n_TOF facility is one of the globally leading Time of Flight neutron beam facilities driven by the CERN PS accelerator. A pulsed proton beam of 20 GeV/c is impinging on a lead spallation target with minimal longitudinal pulse dimension (7 ns rms) allowing for unique energy resolution abilities. n_TOF comprises two TOF beam lines of 185 and 20 m in length. During CERN's 2nd Long Shutdown Phase (LS2) of 2019-2021, a new experimental area, the "NEAR" station, was designed and constructed in close proximity to the target [6]. NEAR Station benefits from an exceptionally high neutron flux, facilitating studies on reactions involving minute sample masses or even radioactive samples with short half-life times. In those cases where the TOF technique is not applicable, the measurement of reaction cross-sections becomes feasible through the utilization of the activation technique. This approach capitalizes on the technique's inherent sensitivity and selectivity, synergizing effectively with NEAR's extremely high neutron flux. As a result, integrated cross section measurements can be conducted, addressing even the most challenging physics cases.

The NEAR Station consists of two sub-areas, an irradiation station, i-NEAR, located next to the target, inside the bunker shielding, and the activation station, a-NEAR, just outside the shielding, at a distance of $\sim$ 3 m. The first one is specifically focused on the radiation hardness studies of materials, while the second one is dedicated to neutron activation reaction studies, primarily for nuclear astrophysics purposes. The neutron beam of the activation station (a-NEAR) is spatially shaped through a hole in the shielding which houses a movable collimating system, composed of stainless steel and borated polyethylene disks. A schematic representation of the above mentioned elements can be found in Fig 1 and more details on the technical characteristics of NEAR can be found in [7]. For nuclear astrophysics studies, the "shaping" of the energy distribution of the low energy neutrons by using appropriate beam filters is feasible, allowing the deduction of Maxwellian Averaged Cross Sections in previously unexplored physics cases.

This work focuses on a-NEAR. In order to establish optimum operation conditions for future experimental activities, the detailed characterization of the newly built experimental area is needed. Accordingly, in this work we describe the procedure and the results of the various experiments carried out in order to investigate its yet unexplored experimental characteristics. Owing to its harsh radiation conditions, conventional in-beam detection systems and electronics could not be employed for the measurement of the neutron flux at a-

[a]e-mail: fauthor@example.com
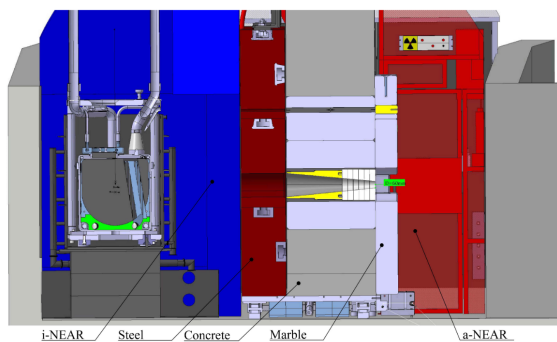
Fig. 1 Schmeatic representation of the NEAR Station elements taken from [7]

NEAR. Instead, a series of multiple foil activation measurements was applied. In the next sections the method, the adopted reference reactions as well as the details on the unfolding procedures are described.

2 Experimental method and setups

2.1 The activation technique

The activation technique, widely acknowledged and potent, finds application across diverse scientific domains and in industrial settings. Its effectiveness stems from its notable attributes: high sensitivity, selectivity, and non-destructive nature. It is based on the ability to identify and quantify radioactive nuclei in a sample based on their unique decay properties, such as type and energy of radiation emitted. Thanks to the advancements in detection setups, the utilization of the activation technique demonstrates significant efficacy in identifying traces within materials and deriving highly accurate results in reaction cross-section measurements, even when minimal sample masses are available (e.g., [8]), or in the characterization of radiation fields when other techniques cannot be applied.

The activation technique is a two-step process: Firstly, the sample is irradiated. During the irradiation one or more nuclear reactions take place. The number and kind of those reactions depends on the energy and the kind of the quanta of the radiation field (e.g. neutron beams, or γ-rays, etc). The activation technique can be applied only if the reaction product of the reaction of interest is an unstable isotope with half-life time ranging between a few seconds up to several years. The second step is the measurement of the induced activity of the sample. The choice of the detection setup depends on the decay properties of the product nuclei i.e. the kind, the intensity and the energy of the emitted radiation.

The applicability of the activation technique is subject to several constrains [9]. Beside the "suitability" of the half-life time of the reaction products, the type of the emitted activity should be considered. Furthermore, potential "contaminating" reaction channels that could populate the same isotope should be taken into account. This can be the case when multi-isotopic natural composition samples are irradiated.

As described in the next sections, within the present work the activation technique was used as to derive the neutron flux and energy distribution of the a-NEAR station. Several reference reactions were used with different thresholds and excitation functions were utilized towards the detailed characterization of the a-NEAR. After the irradiation the activity of the samples was determined by means of γ-ray spectroscopy.

2.2 MAM1

The experimental campaign at a-NEAR started with the Multi-foilActivation Measurement 1, "MAM1", set-up, one out of two set-ups designed for activation measurements. The final configuration of MAM1 comprises several materials, such as Au, Cd, Ni, Sc, and W, with the purpose of covering the eleven orders of magnitude in neutron energy available at the experimental NEAR area. The samples were in the form of metallic foils, while the choice of the reaction channels was based on the resonances as well as the half-life of each produced radionuclide. The samples were placed in different positions inside a disk shaped holder with a radius of 2cm, thus ensuring, according to extended FLUKA simulations, the homogeneity of the NEAR 2D spatial distribution/profile across all samples. The placement of the holder and the samples at a-NEAR during the irradiation is depicted in Fig. 2 while the placement of the samples in the different slots of the holder can be seen in in Fig. ... Stella. The table 1, summarizes the list of the adopted neutron-induced reactions, which consists of six capture reactions, ideal for the characterization of thermal and epithermal energy regions, and eleven threshold reactions, dedicated to the unfolding of the fast neutron energy region. The induced activity of each foil was measured utilizing a well-characterized HPGe detector with a relative efficiency of 26% according to a dedicated measurement plan. A representative γ-ray spectrum of the induced activity of the irradiated samples (Au sample in this instance) can be seen in Fig. 6. More details on the γ-ray spectroscopy are given in Section .... The output results of the analysis procedure were used as an input file to the BATMAN code for the unfolding procedure, a procedure that will be explained in detail in sections XXX.
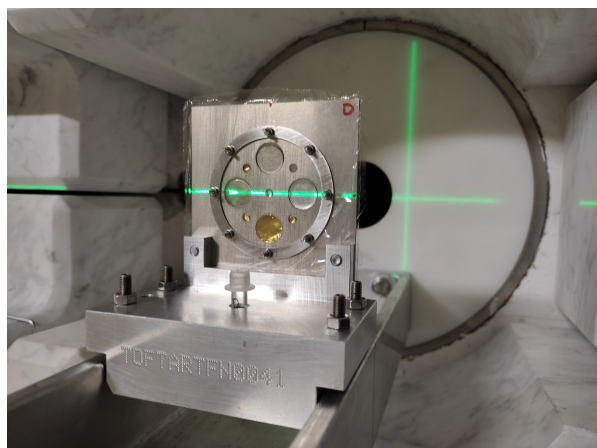
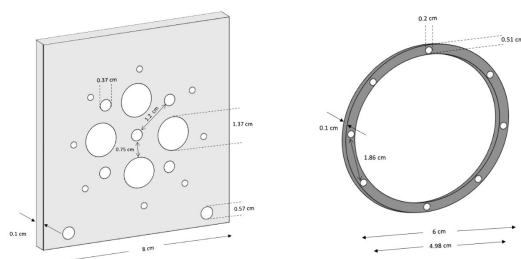**Fig. 2** Photograph taken while aligning the MAM1 sample holder in front of the collimator exit.
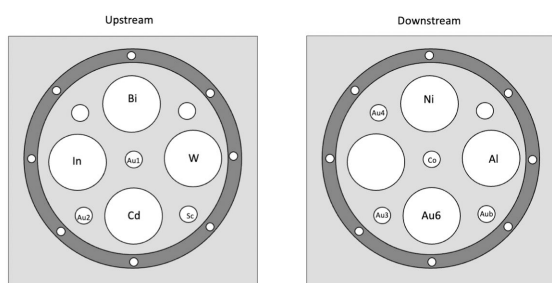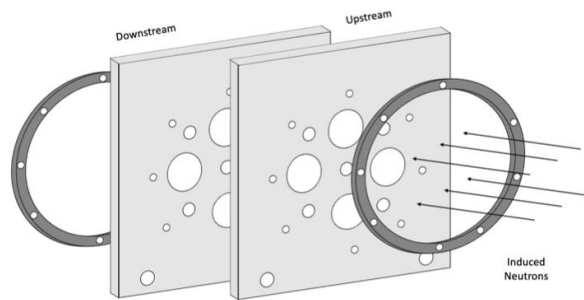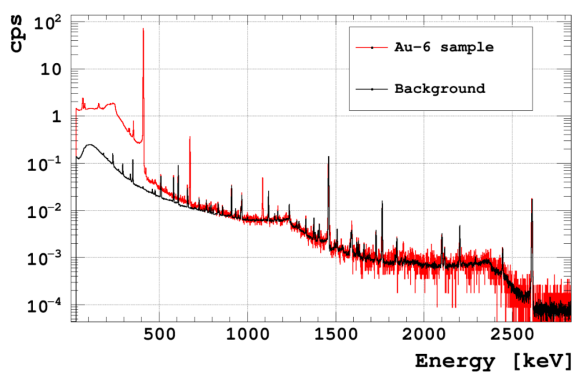

FIGURE 2.4. Holder dimensions.

Fig. 3 MAM1 holder and dimensionsCHOOSE WHATEVER YOU PREFER

Fig. 4 MAM1 holder and dimensionsCHOOSE WHATEVER YOU PREFER

Fig. 5 MAM1 holder and dimensionsCHOOSE WHATEVER YOU PREFER

Fig. 6 Example of a typical γ-ray spectrum. In red: The spectrum resulting from the sample measurement. In black: The background spectrum.

Table 1 MAM1 list of reactions

Sample ID	Mass [g]	Reactions studied
Cd	1.0714	^{114}Cd(n,γ)^{115}Cd
Sc	0.0073	^{45}Sc(n,γ)^{46}Sc
Au-1	0.0709	^{197}Au(n,γ)^{198}Au, ^{197}Au(n,2n)^{196}Au, ^{197}Au(n,4n)^{194}Au
Au-2	0.0712	^{197}Au(n,γ)^{198}Au, ^{197}Au(n,2n)^{196}Au, ^{197}Au(n,4n)^{194}Au
Au-6	0.0550	^{197}Au(n,2n)^{196}Au
Au-3	0.0142	^{197}Au(n,γ)^{198}Au, ^{197}Au(n,2n)^{196}Au
Au-4	0.0149	^{197}Au(n,γ)^{198}Au, ^{197}Au(n,2n)^{196}Au
Au-b	0.0148	^{197}Au(n,γ)^{198}Au, ^{197}Au(n,2n)^{196}Au
W	1.2349	^{186}W(n,γ)^{187}W
In	0.4675	^{113}In(n,γ)^{114}In
Ni	0.5624	^{58}Ni(n,p)^{58}Co, ^{58}Ni(n,2n)^{57}Ni
Al	0.1694	^{27}Al(n,α)^{24}Na
Co	0.0348	^{59}Co(n,γ)^{60}Co, ^{59}Co(n,2n)^{58}Co, ^{59}Co(n,3n)^{57}Co
Bi	1.1070	^{209}Bi(n,3n)^{207}Bi, ^{209}Bi(n,4n)^{206}Bi, ^{209}Bi(n,5n)^{205}Bi

2.3 MAM2

The second set-up designed for Multi-foil Activation Measurements "MAM2", was configured using a different set of samples and positioning compared to MAM1. Several materials, including Au, Co, Sc, In and Al were used. Four capture reactions were used to cover the thermal and epithermal region, and twelve threshold reactions to cover the fast neutron energy region. The full list of reactions used is summarized in Table 2. All the samples were in the form of metallic foils of 0.635 cm radius. A set of foils was placed at the central posi-

tion (aligned with the beam collimator) in a stack configuration. Special care was taken to account for the beam attenuation and self-shielding corrections along each sample within the stack. A second set of Au samples was placed downstream the neutron beam in positions around the center (edges and corners) in order to test the homogeneity of the beam at 2.5 (edges) and 3.5 cm (corners) from the beam axis. The setup can be seen in Fig 7. The irradiated samples were analyzed after irradiation using the same HPGe detector as the MAM1. The activation data was further taken as input to the unfolding routine described in section 3.2.

Table 2 MAM-2 list of reactions. All the Au samples labeled with number correspond to the homogeneity analysis.

Sample ID	Mass [g]	Reactions studied
Au-u	0.1268	^{197}Au(n,γ)^{198}Au, ^{197}Au(n,2n)^{196}Au, ^{197}Au(n,4n)^{194}Au
Co	0.0644	^{59}Co(n,γ)^{60}Co, ^{59}Co(n,2n)^{58}Co, ^{59}Co(n,3n)^{57}Co, ^{59}Co(n,4n)^{56}Co, ^{59}Co(n,p)^{59}Fe
Sc	0.0503	^{45}Sc(n,γ)^{46}Sc
In	0.1309	^{113}In(n,3n)^{111}In, ^{113}In(n,4n)^{110}In, ^{115}In(n,n')^{115m}In
Al	0.2552	^{27}Al(n,α)^{24}Na
Au-d	0.1283	^{197}Au(n,γ)^{198}Au, ^{197}Au(n,2n)^{196}Au, ^{197}Au(n,4n)^{194}Au
Au-1	0.1167	
Au-2	0.1213	
Au-3	1.1154	
Au-4	0.1214	^{197}Au(n,γ)^{198}Au,
Au-6	0.1257	^{197}Au(n,2n)^{196}Au,
Au-7	0.1250	^{197}Au(n,4n)^{194}Au
Au-8	0.1243	
Au-9	0.1222	

2.4 The activity measurement setup, Nikolas

After the irradiation of the samples, the induced activity was measured by means of a High Purity Ge (HPGe) detector. Specifically, a p-type electrically cooled coaxial HPGe detector was used with relative efficiency 27%. The active volume of the HPGe detector was 133 cm^2 and its entrance window is made of thin Aluminium. The high energy resolution of the detector (0.2% at 1.3 MeV) was instrumental in this work providing the needed selectivity and resolution for the identification of the characteristic γ-rays emitted from each reaction product. The sample-to-detector distance was op-
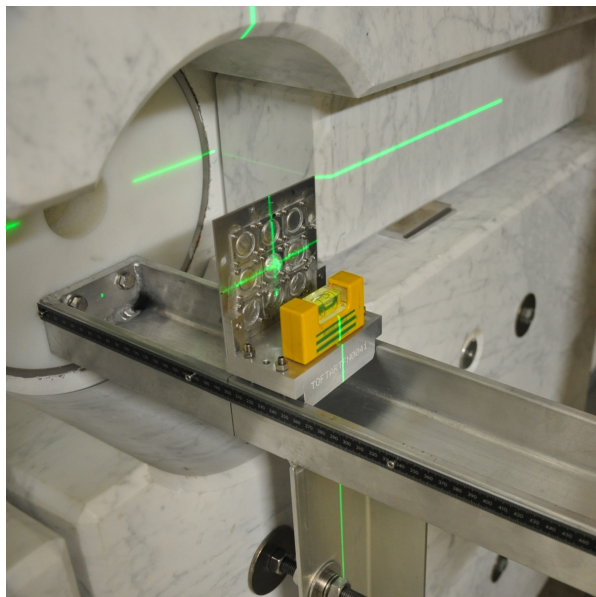
Fig. 7 Photograph taken while aligning the MAM2 sample holder in front of the collimator exit.
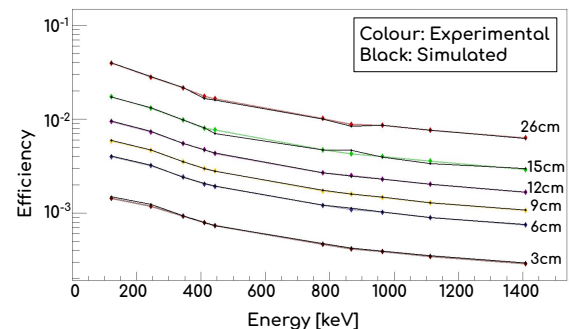
Fig. 8 In colour: Experimentally extracted detection efficiency values. In black: Simulated results.

timized for each measurement as to achieve adequacy statistical uncertainty retaining also low enough counting rates as to avoid possible dead-time or pile-up issues. Thanks to a carefully designed system of spacers a well defined and fully reproducible measurement geometry was achieved. The HPGe detector together with the spacers can be seen in Fig. 9.

For each measurement position the efficiency of the detector was determined using several point-like calibration sources. Furthermore, the HPGe detector was fully modelled and characterized using the GEANT4 simulation toolkit [10,?]. Specifically, starting from the manufacturer detector geometrical characteristics minimal modifications were done in some of the parameters as to reproduce the experimentally deduced efficiency curves for all possible source to detector distances. In Fig... ... Elisso the experimentally deduced detection efficiency along with the corresponding one from the GEANT4 Monte-Carlo simulations is given. Having en-

Fig. 9 The HPGe used for the induced activity measurements of this study. Different polyethylene spacers can also be seen.

sured that the GEANT4 modelling is fully reproducing the experimentally deduced calibration points within 3-5 % the detection efficiency of each sample was eventually obtained from dedicated GEANT4 simulations where the full decay scheme was considered along with details of the structural characteristics of the sample (dimensions, composition, density, etc). In this way, the effect in the detection efficiency due to the extended source geometry, possible γ-ray self attenuation or possible coincidence summing effects were taken into account.

3 Unfolding techniques and codes

- BaTMAN (Davide Chiesa, Mario)
- SAND II (Roza, Maria)
- Granada code (Pablo, Javier)

The second step of the analysis concerns the neutron flux spectrum unfolding. To this aim different unfolding codes has been used, namely BaTMAN (Bayesian unfolding Toolkit for Multi-foil Activation with Neutrons), SAND II (Spectrum Analysis by Neutron Detectors II) and the "home made" Granada-code.

3.1 BaTMAN Code

The Bayesian-unfolding Toolkit for Multi-foil Activation with Neutrons (BaTMAN) [11] has been developed since 2012 to unfold the neutron flux from activation data with a Bayesian statistical approach. This tool has been implemented and validated through a neutron activation campaign at the TRIGA Mark II reactor in Pavia [12,13], and subsequently applied to characterize the neutron fluxes at spallation source beamlines [14, 15] and at the TRIGA RC-1 reactor in Rome [16]. The unfolding procedure aims at determining the neutron flux energy distribution $\varphi(E) = d\phi/dE$ from the measurement of the activation rates R_j of different reactions:

$$R_j = \mathcal{N}_j \int \sigma_j(E)\,\varphi(E)\,f_j(E)\,dE \qquad (1)$$

where $\sigma_j(E)$ is the activation cross section and $\mathcal{N}_j$ are the target nuclei for the reaction j in the activation foil, and $f_j(E)$ is a corrective factor taking into account the self-shielding effect of the samples. The BaTMAN unfolding algorithm solves the following system of linear equations obtained by discretizing the integral in Eq. 1 into n energy groups:

$$\frac{R_j}{\mathcal{N}_j} = \sum_{i=1}^{n} \sigma_{ij}\phi_i \qquad (2)$$

where $\phi_i = \int_{E_i}^{E_{i+1}} \varphi(E)\,dE$ are the unknown variables of the system, and σ_{ij} are the *effective* cross sections calculated in the range of each energy group:

$$\sigma_{ij} = \frac{\int_{E_i}^{E_{i+1}} \sigma_j(E)\,\varphi(E)\,f_j(E)\,dE}{\int_{E_i}^{E_{i+1}} \varphi(E)\,dE} \qquad (3)$$

The BaTMAN toolkit takes in input the activation rates and cross sections with their uncertainties, a *guess* spectrum to compute the *effective* cross sections, and a list of energies to define the group boundaries. A C++ code is used to process the input data, write the Bayesian statistical model and the launch script for the JAGS (Just Another Gibbs Sampler) software [17,18], which runs Markov Chain Monte Carlo (MCMC) simulations to sample the *joint Posterior* probability density function $p(\phi_i|R_j,\sigma_{ij})$. BaTMAN also provides tools for the post-processing of the JAGS output files and for the analysis of the neutron flux unfolding results. In particular, the probability density functions of ϕ_i variables and the correlations among them are obtained by marginalizing the multi-dimensional Posterior. Compared to other unfolding techniques [19], the BaTMAN unfolding method allows to propagate the experimental uncertainties of the activation rates and cross sections, to set Priors

that automatically exclude the meaningless negative solutions for ϕ_i, and to analyze the correlations between the resulting ϕ_i. It is worth noting that even if the results have some degree of dependence on the *intra-group* spectral shape used for σ_{ij} calculation, there is no constraint on ϕ_i variables, that are left free to converge on any flux value in the positive range.

Pointwise cross-section data retrieved in the ENDF/B-VIII.0 and TENDL-2019 libraries for effective cross-section (σ_{ij}) calculations were used for capture reactions, while for the threshold reactions only those published in the TENDL database were used. As cross sections in TENDL database extend up to 30MeV, a linear extrapolation above this energy extends the cross sections up to 200MeV (?see this point?).

The flux attenuation through the samples thickness was taken into account with the self-shielding factor $f_j(E)$ by using the FM card of Monte Carlo N-Particle code (MCNP); the bin-by-bin ratio between the activation rate spectra as a function of neutron energy and those calculated with any perturbations on the neutron flux provided the self-shielding correction factors for all the samples used. As an example in Fig. 11 the f_j factor for the gold sample Au-1 is shown (?placed at the center of samples support?); the self-shielding effect is clearly visible in correspondence of the main resonances @ 4.9eV of the n + ^{197}Au cross section.

As for the others unfolding code used in this work, the starting point is the guess (seed) neutron spectrum; such a flux shown in Fig. 10 was obtained by specifics FLUKA MC simulations (see section...).
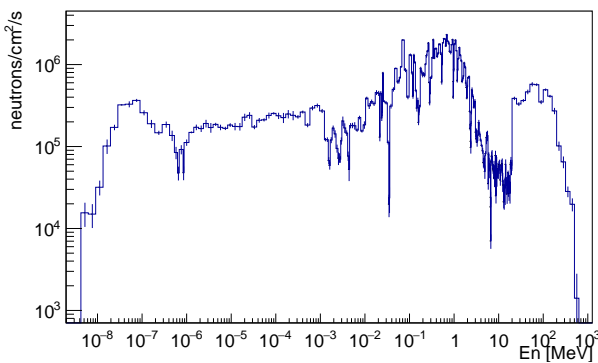
Fig. 10 NEAR neutron flux as obtained by FLUKA MC simulations.

In order to obtain group flux intensities (ϕ_i) as uncorrelated as possible among to them, the multi-group binning of the neutron energy spectrum was chosen in such a way to have at least a main resonance of a capture or a cross section peak of a threshold reaction for each group. To do this the neutron energy range was divided in 8 multi-group binning as reported in Table 3; in total 15 different reactions were measured, namely 6 capture and 9 threshold reactions.
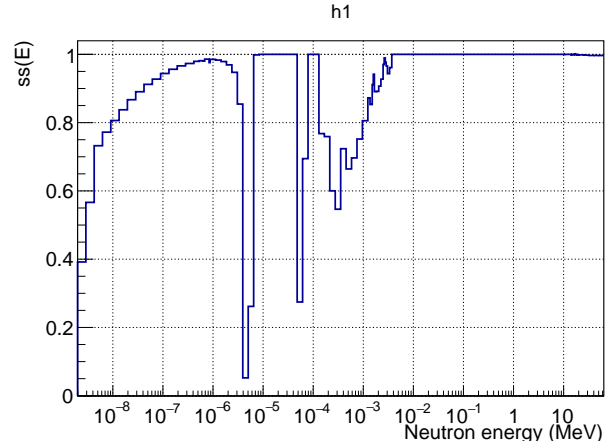
Fig. 11 Self-shielding factor as a function of neutron energy for the gold sample Au-1 as obteined from MCNP simulations of reaction rates.

Table 3 Energy group binning spanning from 1.98meV to 631.60MeV.

Group	Energy range [MeV]
1	1.976e-09 - 1.317e-07
2	1.317e-07 - 3.727e-05
3	3.727e-05 - 4.540e-04
4	4.549e-04 - 1.111e-01
5	1.111e-01 - 6.873e+00
6	6.873e+00 - 1.000e+01
7	1.000e+01 - 3.169e+01
8	3.169e+01 - 6.316e+02

3.2 SAND II

Following the MAM1 foil irradiation that was carried out between the 28th of September and the 20th of October 2021 and the corresponding spectrum analysis, the unfolding SAND II (Spectrum Analysis by Neutron Detectors II) code, initially maintained by the Radiation Shielding Information Center, Oak Ridge National Laboratories and extensively used with great success in nuclear reactors for several decades, was implemented for the determination of the neutron flux, in the energy range between 10-10 and 18 MeV [**?**]. The SAND II code is currently provided by the NEA Data Bank and has been developed specifically for the neutron spectrum de-convolution when the neutron activation tech-

nique is used. The code employs an iterative perturbation method to obtain a "best fit" neutron flux spectrum for a given input set of experimental saturated activities from the irradiated foils, yielding the necessary information for the neutron flux characterization, within the energy range of each threshold and capture nuclear reaction. Accurate group cross sections from the IRDFF library, for each reaction and for each SAND II energy interval, are implemented in the code, along with an initial "guessed" flux spectrum (i.e. 'seed spectrum'). The algorithm subsequently adjusts iteratively the neutron flux spectrum to achieve an appropriate fit between the theoretically calculated and the experimentally determined reaction rates, within the energy range of 0-18 MeV, divided into 620 intervals. The exact determination of the 620 interval values with a small number of measured activities creates a non-inverse matrix problem, since each activity used as input represents an equation of 620 unknown values. In this work, only 12 saturated activities were used, thus the determination of 620 intervals using only 12 equations was a rather difficult task considering the limitations of the neutron-induced reactions. Thus, a carefully chosen initial seed neutron spectrum was used, derived from extensive FLUKA [20][21][22] simulations carried out at CERN [23]. A test has been performed to investigate the sensitivity of the code to the initial flux spectrum, implementing four different neutron flux spectra, as will be described below. In addition, a moving linear averaging factor was adopted by means of the smoothing factor parameter N_s. It is evident that an increase in the N_s parameter causes a relative loss of all the information which is related to the fine structure of the neutron flux provided by the seed spectrum. In the final results a smoothing factor limited to a value of 5 has been adopted.

The neutron flux spectrum obtained using the SAND II code is presented in Fig. 12 as blue line along with the initial seed flux spectrum from the FLUKA simulations (black line). The two neutron spectra are in a very good agreement over the whole energy range, from the thermal up to the MeV region, while above 4 MeV, the calculated neutron flux is significantly higher than the simulated one. The experimental and calculated saturated activities per target nucleus (in Bq/TN) and their standard deviations for every reaction of the data set, are shown in Table 4. The resulting spectrum presented in Fig. 12, seems to provide a very good estimation of the realistic neutron flux, as the code calculated saturated activities are within a total standard deviation of 5.24% from the measured ones. The energy regions where the 12 reactions used in this work are important for the neutron spectrum deconvolution process, are shown as red lines in Fig. 13. It is seen that the experimental information in the energy region from 4 to 18 MeV is sufficient to provide a reliable value of the neutron flux, higher than expected from the FLUKA simulations. In order to compare the SAND II results with the ones emanating from the Bayesian code BaTMAN [ref], the same binning has been used (seven bins in total), presented as green lines in comparison with the FLUKA simulations (red lines).

Finally, it should be noted that the threshold saturated activities used as input in the SAND II code, had to be modified to correspond to the specific part of the neutron flux within the energy range between 0 and 18 MeV. This correction factor was crucial to obtain an accurate estimation of the flux in the fast energy neutron region, for all the threshold reactions. For calculation purposes, the FLUKA simulation code was utilized following the equations:

$$\text{From } 10 - 50 MeV : A_1 = \Sigma \sigma_i * \Phi_i * (E_{i+1} - E_i) \quad (3)$$

$$\text{From } 10 - 18 MeV : A_2 = \Sigma \sigma_i * \Phi_i * (E_{i+1} - E_i) \quad (4)$$

$$\frac{A_1}{A_2} * A_{measured} = A_{SANDIIinput}$$

where A corresponds to the threshold saturated activities, $E_{i+1} - E_i$ is the energy interval with respect to the neutron flux Φ_i, and the quantity σ_i is the reaction cross section [24]. It should be also noted that all the relevant correction factors, related to the self-absorption of gamma-rays and the self-shielding of neutrons in the irradiated samples, were obtained from MCNP [25] simulations [26]. The experimental saturated activities per target nucleus shown in Table 1 along with the calculated ones, include all the aforementioned corrections.

In an attempt to test the sensitivity of the code to the initial "guessed" flux spectrum, four different neutron flux spectra were implemented, shown as blue, green and red lines in Fig.14(a), which were related to the FLUKA Monte-Carlo simulation results (black line in Fig. 14(a)). The smoothing factor $Ns = 20$ was found to be the most reliable one among all the others used in this test, due to the clear solution convergence we have managed to achieve between the four different differential flux results within the energy range where most of the saturated activities contributed. The resulting neutron spectra from the SAND II code are presented in Fig. 14(b) using the same colors as the relevant initial neutron spectra and are seen to converge fairly well. Indeed, the significant divergence of the three lines (blue, green and red) in Fig. 14(b) occurs mainly in the region 10keV and 1MeV, where the experimental information provided by the 12 activation reactions used in this work, is not sufficient, as can be seen in Fig. 14. The
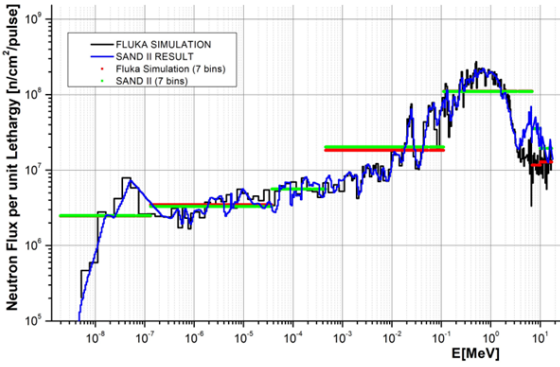
Fig. 12 The SAND-II neutron flux energy spectrum resulting from the unfolding procedure in comparison with the FLUKA simulations using two different energy binning.
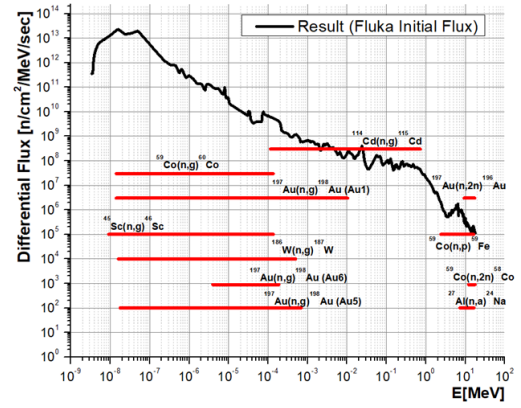

Fig. 13 The red lines indicate the energy regions where the reactions used in this work are important for the neutron spectrum deconvolution process.

Table 4 The saturated experimental and calculated activities along with their standard deviations for the reactions used in this work from the irradiated samples.

Sample	Reaction	Experimental Activity	Calculated Activity	Standard Deviation
Au-1	(n, γ)	$2.995 * 10^{-16}$	$3.152 * 10^{-16}$	-4.99
Au-5	(n, γ)	$4.679 * 10^{-16}$	$5.082 * 10^{-16}$	-7.93
Au-6	(n, γ)	$7.189 * 10^{-16}$	$6.643 * 10^{-16}$	8.22
Au-1	$(n, 2n)$	$2.958 * 10^{-18}$	$3.125 * 10^{-18}$	-5.36
Sc	(n, γ)	$4.426 * 10^{-17}$	$4.204 * 10^{-17}$	5.27
Co	(n, γ)	$7.218 * 10^{-17}$	$7.328 * 10^{-17}$	1.50
Co	$(n, 2n)$	$7.307 * 10^{-19}$	$7.146 * 10{-19}$	2.26
Co	(n, p)	$1.836 * 10^{-19}$	$1.699 * 10^{-19}$	-1.50
W	(n, γ)	$1.836 * 10^{-16}$	$1.855 * 10^{-16}$	-0.14
Ni	(n, p)	$3.871 * 10^{-18}$	$4.029 * 10^{-18}$	-3.93
Al	(n, α)	$2.610 * 10^{-19}$	$2.641 * 10^{-19}$	-1.20
Cd114	(n, γ)	$1.433 * 10^{-17}$	$1.414 * 10^{-17}$	1.28

Total SD: 5.24%
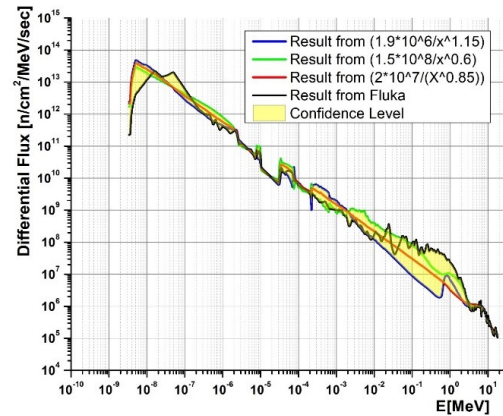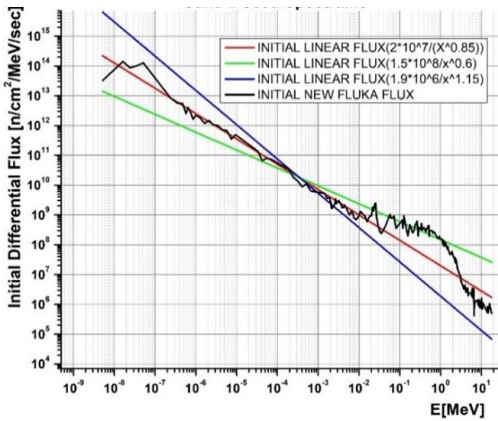
Fig. 14 (a) Representation of the four different initial differential neutron fluxes used as input in the SAND II code (b) Results of the differential neutron flux from the SAND II code using the initial fluxes shown in (a).

clear convergence in the thermal and fast neutron energy region is attributed to the adequate experimental information provided by the threshold and capture activation reactions. The confidence level of this sensitivity test of the code to the initial neutron flux spectrum is also presented in Fig. 14(b) in yellow.

3.3 Granada Code

Table 5 Please write your table caption here

| first	second	third
number	number	number
number	number	number

4 FLUKA simulations (Cecchetto)

Text here...

5 Results (Nicola, Nikolas, Mario, Pablo, Roza)

- MAM1 (BaTMAN), MAM1 (Granada), MAM1 (SAND II), MAM2
- Uncertainties
- Evaluated flux vs Simulated one
- Effect of Cd-114(n,g) cross section

6 Conclusions

References

1. C. Rubbia. A high resolution spallation driven facility at the cern-ps to measure neutron cross sections in the interval from 1 ev to 250 mev: A relative performance assessment (1998)
2. U. Abbondanno, G. Aerts, F. Alvarez-Velarde, H. 'Alvarez-Pol, S. Andriamonje, J. Andrzejewski, G. Badurek, P. Baumann, F. Bečv'ař, J. Benlliure, E. Berthoumieux, F. Calvi no, D. Cano-Ott, R. Capote, P. Cennini, V. Chepel, E. Chiaveri, N. Colonna, G. Cortes, D. Cortina, A. Couture, J. Cox, S. Dababneh, M. Dahlfors, S. David, R. Dolfini, C. Domingo-Pardo, I. Duran, M. Embid-Segura, L. Ferrant, A. Ferrari, R. Ferreira-Marques, H. Frais-Koelbl, W. Furman, I. Goncalves, R. Gallino, E. Gonzalez-Romero, A. Goverdovski, F. Gramegna, E. Griesmayer, F. Gunsing, B. Haas, R. Haight, M. Heil, A. Herrera-Martinez, S. Isaev, E. Jericha, F. K"appeler, Y. Kadi, D. Karadimos, M. Kerveno, V. Ketlerov, P. Koehler, V. Konovalov, M. Krtička, C. Lamboudis, H. Leeb, A. Lindote, I. Lopes, M. Lozano, S. Lukic, J. Marganiec, S. Marrone, J. Martinez-Val, P. Mastinu, A. Mengoni, P.M. Milazzo, A. Molina-Coballes, C. Moreau, M. Mosconi, F. Neves, H. Oberhummer, S. O'Brien, J. Pancin, T. Papaevangelou, C. Paradela, A. Pavlik, P. Pavlopoulos, J.M. Perlado, L. Perrot, M. Pignatari, R. Plag, A. Plompen, A. Plukis, A. Poch, A. Policarpo, C. Pretel, J. Quesada, S. Raman, W. Rapp, T. Rauscher, R. Reifarth, M. Rosetti, C. Rubbia, G. Rudolf, P. Rullhusen, J. Salgado, J.C. Soares, C. Stephan, G. Tagliente, J. Tain, L. Tassan-Got, L. Tavora, R. Terlizzi, G. Vannini, P. Vaz, A. Ventura, D. Villamarin, M.C. Vincente, V. Vlachoudis, F. Voss, H. Wendler, M. Wiescher, K. Wisshak, Phys. Rev. Lett. **93**, 161103 (2004). DOI 10.1103/PhysRevLett.93.161103. URL https://link.aps.org/doi/10.1103/PhysRevLett.93.161103
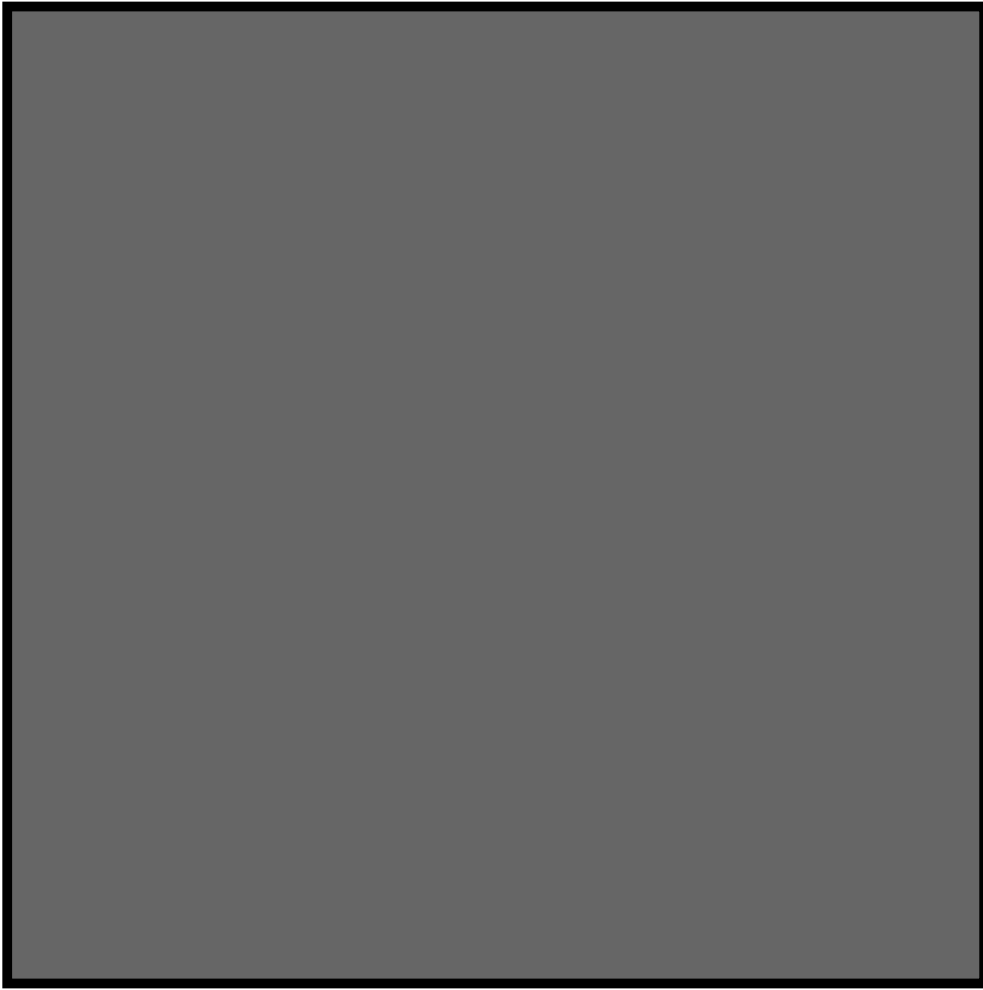
Fig. 15 Please write your figure caption here

3. C. Lederer, C. Massimi, S. Altstadt, J. Andrzejewski, L. Audouin, M. Barbagallo, V. B'ecares, F. Bečv'ař, F. Belloni, E. Berthoumieux, J. Billowes, V. Boccone, D. Bosnar, M. Brugger, M. Calviani, F. Calvi no, D. Cano-Ott, C. Carrapiço, F. Cerutti, E. Chiaveri, M. Chin, N. Colonna, G. Cort'es, M.A. Cort'es-Giraldo, M. Diakaki, C. Domingo-Pardo, I. Duran, R. Dressler, N. Dzysiuk, C. Eleftheriadis, A. Ferrari, K. Fraval, S. Ganesan, A.R. Garc'ıa, G. Giubrone, M.B. G'omez-Hornillos, I.F. Gonçalves, E. Gonz'alez-Romero, E. Griesmayer, C. Guerrero, F. Gunsing, P. Gurusamy, D.G. Jenkins, E. Jericha, Y. Kadi, F. K"appeler, D. Karadimos, N. Kivel, P. Koehler, M. Kokkoris, G. Korschinek, M. Krtička, J. Kroll, C. Langer, H. Leeb, L.S. Leong, R. Losito, A. Manousos, J. Marganiec, T. Mart'ınez, P.F. Mastinu, M. Mastromarco, M. Meaze, E. Mendoza, A. Mengoni, P.M. Milazzo, F. Mingrone, M. Mirea, W. Mondelaers, C. Paradela, A. Pavlik, J. Perkowski, M. Pignatari, A. Plompen, J. Praena, J.M. Quesada, T. Rauscher, R. Reifarth, A. Riego, F. Roman, C. Rubbia, R. Sarmento, P. Schillebeeckx, S. Schmidt, D. Schumann, G. Tagliente, J.L. Tain, D. Tarr'ıo, L. Tassan-Got, A. Tsinganis, S. Valenta, G. Vannini, V. Variale, P. Vaz, A. Ventura, R. Versaci, M.J. Vermeulen, V. Vlachoudis, R. Vlastou, A. Wallner, T. Ware, M. Weigand, C. Weiß, T.J. Wright, P. Žugec, Phys. Rev. Lett. **110**, 022501 (2013). DOI 10.1103/PhysRevLett.110.022501. URL https://link.aps.org/doi/10.1103/PhysRevLett.110.022501

4. N. Colonna, F. Belloni, E. Berthoumieux, M. Calviani, C. Domingo-Pardo, C. Guerrero, D. Karadimos, C. Lederer, C. Massimi, C. Paradela, R. Plag, J. Praena, R. Sarmento, Energy Environ. Sci. **3**, 1910 (2010). DOI 10.1039/C0EE00108B. URL http://dx.doi.org/10.1039/C0EE00108B

5. N. Colonna, et al., EPJ Web Conf. **165**, 01014 (2017). DOI 10.1051/epjconf/201716501014. URL https://doi.org/10.1051/epjconf/201716501014

6. T. n$_T$OFCollaboration, (2020)

7. M. Ferrari, D. Senajova, O. Aberle, Y. Aguiar, D. Baillard, M. Barbagallo, A.P. Bernardes, L. Buonocore, M. Cecchetto, V. Clerc, M.D. Castro, R.G. Alia, S. Girod, J.L. Grenard, K. Kershaw, G. Lerner, M. Maeder, A. Makovec, A. Mengoni, M.P. Ornedo, F. Pozzi, C.V. Almagro, M. Calviani, (2022)

8. N. Patronis, S. Dababneh, P.A. Assimakopoulos, R. Gallino, M. Heil, F. Käppeler, D. Karamanis, P.E. Koehler, A. Mengoni, R. Plag, Physical Review C **69**, 025803 (2004). DOI 10.1103/PhysRevC.69.025803

9. N. Tsoulfanidis, S. Landsberger, *Measurement Detection of Radiation*, 4th edn. (Taylor Francis, 2015)

10. J. Allison, K. Amako, J. Apostolakis, P. Arce, M. Asai, T. Aso, E. Bagli, A. Bagulya, S. Banerjee, G. Barrand, B. Beck, A. Bogdanov, D. Brandt, J. Brown, H. Burkhardt, P. Canal, D. Cano-Ott, S. Chauvie, K. Cho, G. Cirrone, G. Cooperman, M. Cortés-Giraldo, G. Cosmo, G. Cuttone, G. Depaola, L. Desorgher, X. Dong, A. Dotti, V. Elvira, G. Folger, Z. Francis, A. Galoyan, L. Garnier, M. Gayer, K. Genser, V. Grichine, S. Guatelli, P. Guèye, P. Gumplinger, A. Howard, I. Hřivnáčová, S. Hwang, S. Incerti, A. Ivanchenko, V. Ivanchenko, F. Jones, S. Jun, P. Kaitaniemi, N. Karakatsanis, M. Karamitros, M. Kelsey, A. Kimura, T. Koi, H. Kurashige, A. Lechner, S. Lee, F. Longo, M. Maire, D. Mancusi, A. Mantero, E. Mendoza, B. Morgan, K. Murakami, T. Nikitina, L. Pandola, P. Paprocki, J. Perl, I. Petrović, M. Pia, W. Pokorski, J. Quesada, M. Raine, M. Reis, A. Ribon, A. Ristić Fira, F. Romano, G. Russo, G. Santin, T. Sasaki, D. Sawkey, J. Shin, I. Strakovsky, A. Taborda, S. Tanaka, B. Tomé, T. Toshito, H. Tran, P. Truscott, L. Urban, V. Uzhinsky, J. Verbeke, M. Verderi, B. Wendt, H. Wenzel, D. Wright, D. Wright, T. Yamashita, J. Yarba, H. Yoshida, Nuclear Instruments and Methods in Physics Research Section A: Accelerators, Spectrometers, Detectors and Associated Equipment **835**, 186 (2016). DOI https://doi.org/10.1016/j.nima.2016.06.125. URL https://www.sciencedirect.com/science/article/pii/S0168900216306957

11. BaTMAN: Bayesian-unfolding Toolkit for Multi-foil Activation with Neutrons. https://github.com/davidechiesa/BaTMAN. Accessed: 2024-01-09

12. A. Borio di Tigliole, A. Cammi, D. Chiesa, M. Clemenza, S. Manera, M. Nastasi, L. Pattavina, R. Ponciroli, S. Pozzi, M. Prata, E. Previtali, A. Salvini, M. Sisti, Progress in Nuclear Energy **70**, 249 (2014)

13. D. Chiesa, E. Previtali, M. Sisti, Annals of Nuclear Energy **70**, 157 (2014)

14. D. Chiesa, M. Nastasi, C. Cazzaniga, M. Rebai, L. Arcidiacono, E. Previtali, G. Gorini, C.D. Frost, Nucl. Instrum. Meth. A **902**, 14 (2018). DOI 10.1016/j.nima.2018.06.016

15. D. Chiesa, C. Cazzaniga, M. Nastasi, M. Rebai, C.D. Frost, G. Gorini, S. Lilley, S. Pozzi, E. Previtali, IEEE Trans. Nucl. Sci. **69**(7), 1659 (2022). DOI 10.1109/TNS.2021.3138636

16. D. Chiesa, et al., Eur. Phys. J. Plus **135**(4), 349 (2020). DOI 10.1140/epjp/s13360-020-00334-7

17. M. Plummer, Proceedings of the 3rd International Workshop on Distributed Statistical Computing (DSC 2003); Vienna, Austria. (2003)

18. M. Plummer, *JAGS Version 3.3.0 User Manual* (2012)

19. M. Reginatto, Radiat. Meas. **45**(10), 1323 (2010). DOI 10.1016/j.radmeas.2010.06.016

20.

21.

22.

23.

24.

25.

26.